Critical analysis of proximity-induced magnetism in $MnTe/Bi_2Te_3$ heterostructures

G. Awana,[1,*] R. Fujita,[2,*] A. Frisk,[3] P. Chen,[4] Q. Yao,[5] A. J. Caruana,[6] C. J. Kinane,[6] N.-J. Steinke,[7] S. Langridge,[6] P. Olalde-Velasco,[3,†] S. S. Dhesi,[3] G. van der Laan,[3] X. F. Kou,[8] S. L. Zhang,[5] T. Hesjedal,[2] and D. Backes[3,‡]

[1]*Department of Physics, Loughborough University, Loughborough LE11 3TU, United Kingdom*
[2]*Department of Physics, Clarendon Laboratory, University of Oxford, Oxford OX1 3PU, United Kingdom*
[3]*Diamond Light Source, Harwell Science and Innovation Campus, Didcot OX11 0DE, United Kingdom*
[4]*School of Information Science and Technology, ShanghaiTech University, Shanghai 200031, China*
[5]*School of Physical Science and Technology, ShanghaiTech Laboratory for Topological Physics, ShanghaiTech University, Shanghai 200031, China*
[6]*ISIS, Rutherford Appleton Laboratory, Harwell Science and Innovation Campus, Science and Technology Facilities Council, Oxon OX11 0QX, United Kingdom*
[7]*Institut Laue-Langevin, 38042 Grenoble Cedex 9, France*
[8]*School of Information Science and Technology and ShanghaiTech Laboratory for Topological Physics, ShanghaiTech University, Shanghai 200031, China*

(Received 26 January 2022; revised 18 March 2022; accepted 25 April 2022; published 11 May 2022)

An elegant approach to overcome the intrinsic limitations of magnetically doped topological insulators is to bring a topological insulator in direct contact with a magnetic material. The aspiration is to realize the quantum anomalous Hall effect at high temperatures where the symmetry-breaking magnetic field is provided by a proximity-induced magnetization at the interface. Hence, a detailed understanding of the interfacial magnetism in such heterostructures is crucial, yet its distinction from structural and magnetic background effects is a rather nontrivial task. Here, we combine several magnetic characterization techniques to investigate the magnetic ordering in $MnTe/Bi_2Te_3$ heterostructures. A magnetization profile of the layer stack is obtained using depth-sensitive polarized neutron reflectometry. The magnetic constituents are characterized in more detail using element-sensitive magnetic x-ray spectroscopy. Magnetotransport measurements provide additional information about the magnetic transitions. We find that the supposedly antiferromagnetic MnTe layer does not exhibit an x-ray magnetic linear dichroic signal, raising doubt that it is in its antiferromagnetic state. Instead, Mn seems to penetrate into the surface region of the Bi_2Te_3 layer. Furthermore, the interface between MnTe and Bi_2Te_3 is not abrupt, but extending over $\sim$2.2 nm. These conditions are the likely reason that we do not observe proximity-induced magnetization at the interface. Our findings illustrate the importance of not solely relying on one single technique as proof for proximity-induced magnetism at interfaces. We demonstrate that a holistic, multitechnique approach is essential to gain a more complete picture of the magnetic structure in which the interface is embedded.

DOI: 10.1103/PhysRevMaterials.6.053402

I. INTRODUCTION

The quantum anomalous Hall (QAH) effect has been predicted [1] and experimentally confirmed in magnetic topological insulators (TIs) [2]. The breaking of time-reversal symmetry by the intrinsic magnetic field in the magnetic TI induces a band gap in the normally ungapped Dirac states [3], leaving only the edges at the border of the surfaces as one-dimensional conductance paths. Transport in QAH systems is characterized by quantization of the transverse resistivity of $\hbar/e^2$ and zero longitudinal resistivity, ideal for dissipationless electronic circuits and energy efficient devices. Such currents are fully spin-polarized and protected by the topology, rendering them attractive for spintronics applications. Combined with superconductors, chiral Majorana edge states can be generated [4]—an approach which could be transformative for future quantum computing [5].

In contrast to the quantum Hall effect [6], no large external magnetic fields are required to observe the QAH effect. Instead, the magnetic field is intrinsically provided via long-range magnetic order in the TI [2,7–12] or by placing a magnetic layer in close proximity to the TI [13–16]. So far, the QAH effect has been observed in Cr- and V-doped $(Sb, Bi)_2Te_3$ [2,7,9] and in the intrinsic magnetic TI $MnBi_2Te_4$ [17]. The required temperatures to observe this

*G. Awana and R. Fujita contributed equally to this work.
†Present address: Departamento de Ciencias Químicas, Universidad Nacional Autónoma de México, Cuautitlán Izcalli, 54740, México.
‡dirk.backes@diamond.ac.uk

phenomenon are <1 K, although the topological surface states (TSSs) persist up to above room temperature. One reason for the low temperatures is that the magnetic order prevails only up to ∼30 K. But more importantly, the magnetic dopants act as defects in the semiconducting TI materials, leading to inhomogeneities in the coupling between TSS and the induced magnetic moment [18]. This causes spatial fluctuations of the induced band gap of the TSS, i.e., reducing the effective band gap of the QAH system and thereby decreasing its operating temperature [19].

Proximity-induced magnetization (PIM) has the advantage of instilling a magnetic field without mixing the TI with the magnetic material. Since the TI is spatially separated from the magnetic material, the disadvantages related to doping should be circumventable. Although PIM in EuS/Bi_2Se_3 has been reported [16], the observation of the QAH effect has remained elusive in these material systems. On the other hand, by using (Zn,Cr)Te as the insulating ferromagnet, traces of the QAH effect were found in large magnetic fields [20]. The difficulty of probing the QAH in ferromagnetic insulator (FMI)/TI-systems might be related to the inherent properties of the FMI adlayer being used, i.e., strong magnetic stray fields which interfere with the TI, thus making probing and optimization of the PIM in the TI very difficult. One way to avoid the detrimental effects of stray fields is to replace the ferromagnet with an antiferromagnet (AFM). If the antiferromagnetic order is collinear, the uncompensated layer terminating the AFM, and sharing an interface with the TI, acts in the same way as its FM counterpart [21]. So far, exchange coupling has been observed at the interface of the AFM CrSb sandwiched between the two magnetically doped TI Cr-doped $(Bi, Sb)_2Te_3$ [22]. Here, the AFM mediates an antiparallel magnetization orientation between the ferromagnetic TIs and stabilizes their magnetic order, manifesting itself in a higher Curie temperature (T_C) compared to a single Cr-doped $(Bi, Sb)_2Te_3$ layer. Signatures of the geometric Hall effect were found in bilayers of the AFM MnTe and the TI $(Bi, Sb)_2Te_3$ [23]. Antisymmetric spikes in the magnetoresistance during reversal were observed in sandwich structures of the nonmagnetic TI $(Bi, Sb)_2Te_3$ and the AFM CrSb [24]. A detailed study of the spin structure of AFM/TI heterostructures, in particular, of their interfacial magnetization, as has been carried out for FMI/TI interfaces, is still lacking.

Here, we combine magnetotransport, polarized neutron reflectometry (PNR) and magnetic x-ray spectroscopy to gain a comprehensive understanding of the magnetization of $MnTe/Bi_2Te_3$ heterostructures and their interfaces. A nonvanishing magnetic moment was detected in the CrSe seed layer with indications for a nonvanishing magnetic moment in both the bulk of the sample and the surface region of the nonmagnetic TI Bi_2Te_3 at 3 K. However, the latter two moments are small and within the statistical error of the PNR measurements. The potential origins, such as diffusion of magnetic constituents, interface roughness, alloying, and structural changes will be discussed against the background of additional insight from magnetotransport and element-sensitive magnetic x-ray spectroscopy. The combined knowledge about the material system gives rise to a reliable model for its magnetic depth profile, from which a PIM effect at the interface between Bi_2Te_3 and MnTe can be excluded, highlighting the importance of a complementary, multimethod approach.

II. SAMPLE GROWTH

Substrate/CrSe/$MnTe/Bi_2Te_3$ samples with GaAs(111)B as substrates were grown using molecular beam epitaxy (MBE), as described in more detail in Ref. [25]. The native oxide layer on the epiready, semi-insulating GaAs(111)B substrate was removed by annealing the wafer at 570°C in a Se atmosphere. A CrSe layer was deposited at 180°C on the GaAs substrate as a seed layer for the MnTe layer.

MnTe and the TI Bi_2Te_3 were grown by codeposition from effusion cells at 370 °C and 200 °C, respectively. Note that the Bi_2Te_3 growth temperature is much lower than the growth temperature for MnTe, thereby minimizing the possible diffusion of Mn into Bi_2Te_3 during the growth process. The thicknesses were measured by x-ray reflectivity with the MnTe and the Bi_2Te_3 layer being (32 ± 1) nm and (15 ± 1) nm thick, respectively. Reflection high-energy electron diffraction was employed to monitor the quality of the layers *in situ* during growth, while transmission electron microscopy, x-ray diffraction, and reflectivity were carried out *ex situ* to confirm the crystal structure and quality, and to determine the sample thickness [25].

III. MAGNETOTRANSPORT

The $CrSe/MnTe/Bi_2Te_3$ films were patterned into Hall bars and transport measurements were carried out in a four-terminal setup down to a temperature of 1.5 K with the magnetic field applied out of plane [see insert in Fig. 1(a)]. Transverse resistance plots (R_{xy}) are shown in Fig. 1, for which a linear background, stemming from the ordinary Hall effect, has been subtracted. Using the ordinary Hall resistance, the carrier density was found to be -2.0×10^{14} cm^{-2} and dominated by n-type charge carriers. Both the MnTe and Bi_2Te_3 layers are conductive, and it has to be pointed out that the measured carrier density represents the overall carrier density of the multilayer. The hysteresis is a superposition of the anomalous Hall effect (AHE) of the MnTe and Bi_2Te_3 layers. In line with earlier reports on $CrSe/MnTe/Bi_2Te_3$ [25] and $CrSe/MnTe/(Bi, Sb)_2Te_3$ layers [23], the signal is composed of the contributions from the MnTe layer on the one hand and the Bi_2Te_3 or $(Bi, Sb)_2Te_3$ layer on the other hand, while CrSe as an insulator does not have any direct impact on the transport [25]. The two AHE contributions have opposite signs, leading to the distorted shape of the hysteresis observed. Contributions with the same sign were observed in Ref. [23], where an antiferromagnetic state of MnTe was reported. As will be demonstrated in the subsequent x-ray spectroscopy measurements, signatures of antiferromagnetism in MnTe could not be observed. Hence, a different magnetic state of the MnTe layer could be an explanation for the deviating transport behavior.

Three temperature regimes can be distinguished, which are shown in the different panels in Fig. 1. At the lowest temperature, the high field amplitudes of the two AHE contributions are similar in value but opposite in sign, resulting in a total resistance of about zero [see Fig. 1(a)]. With increasing temperature, the AHE contribution of Bi_2Te_3 decreases. This has

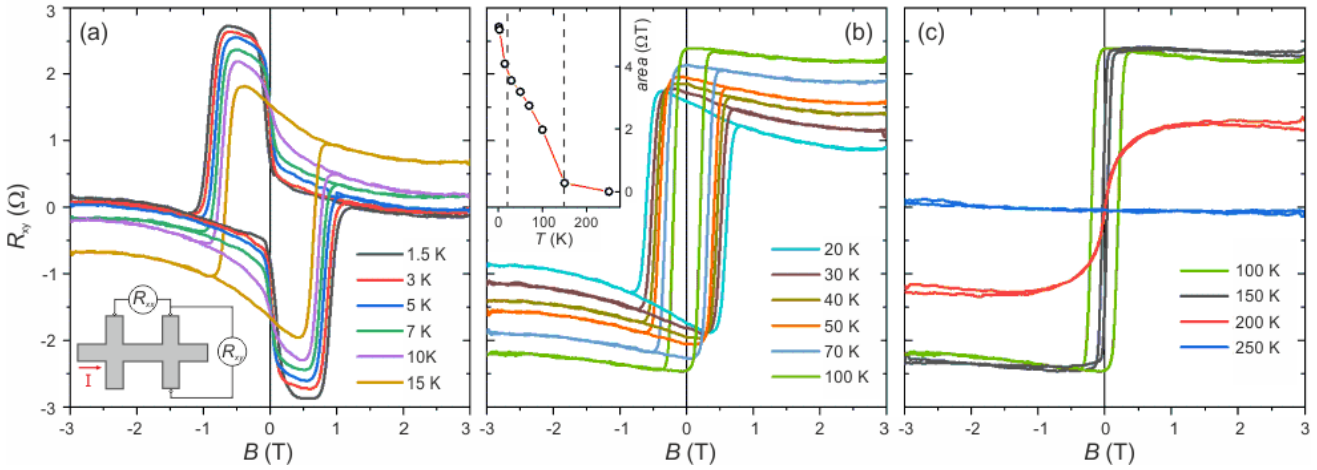

FIG. 1. Plots of the Hall resistance R_{xy} in different temperature regimes. The hysteresis is due to the AHE effect and obtained after subtracting a linear background due to the ordinary Hall effect. In (a), the low temperature data is shown, which is governed up to 10 K by a two-step behavior. The insert shows the geometry of the resistance measurement. The higher temperature data shown in (b) and (c) is dominated by an increasingly square hysteresis loop, which rounds off between 150 and 200 K and finally vanishes between 200 and 250 K. The inset in (b) shows the areas enclosed by the hysteresis loops as a function of temperature.

two implications: First, the humps in the AHE hysteresis get smaller in size and disappear between 10 and 15 K. Second, the resistance at high magnetic fields continuously increases with rising temperature. A decrease of the coercivity sets in and continues while warming up. Above 15 K, the humps due to the Bi_2Te_3 contribution have vanished completely, but a deviation of the MnTe hysteresis from its regular square shape is still visible. Furthermore, the saturation region for fields larger than 1 T is nonlinear. This effect lasts up to a temperature between 100 and 150 K [see Fig. 1(b)]. However, whether its origin is the same as for the humps is not clear. Above 150 K, the coercivity of the AHE hysteresis is considerably reduced. At higher temperatures, the shape changes from square-shaped to a more rounded form, which is an indication of a weakening of the magnetic anisotropy and the most likely reason for the decrease in coercivity [see Fig. 1(c)]. Between 200 and 250 K, the AHE hysteresis has disappeared, resulting from the vanishing MnTe contribution.

These temperature regimes are also visible when the areas enclosed by the hysteresis loops are plotted as a function of temperature [see inset in Fig. 1(b)]. Here, the slope is very steep below 15 K because of the vanishing contribution of the Bi_2Te_3 layer to the AHE. The change in loop area at temperatures larger than 15 K is due to the narrowing of the MnTe hysteresis, making it impossible to detect changes above 150 K.

IV. POLARIZED NEUTRON REFLECTOMETRY

To determine the spatial distribution of magnetic order in the heterostructure, we performed PNR measurements on the POLREF instrument at the ISIS Muon and Neutron Source (Oxfordshire, UK). The data was collected over a wave-vector range of $0.008 < Q < 0.12\,\text{Å}^{-1}$. An in-plane magnetic field of 0.7 T was applied to align the magnetization colinear with the polarization vector of the beam and, consequently, in the same direction as the neutron spin. The Fresnel PNR data and the nuclear scattering length density (nSLD) profiles are shown in Fig. 2. More information on the modeling to obtain a good nSLD profile can be found in the Supplemental Material [26].

The 3 and 300 K data sets were co-refined using a shared nSLD profile, whereas the magnetic profiles were allowed to vary independently at each temperature. Three different magnetic models were considered, where the nSLD profiles were allowed to change independently between them (see Fig. 3). However, as can be seen in the tables in the Supplemental Material [26] as well, the nSLD profiles varied only fractionally—an indication that the nuclear structure of the sample is very well defined. There are four main points to take from the nSLD profiles displayed in Fig. 2.

First, a good fit to the data could only be obtained by introducing a thick GaAs buffer layer to the system. This is in agreement with atomic force microscopy imaging of the sample, showing that the substrate was very granular in nature (see Supplemental Material [26] for further details).

Second, the CrSe layer nSLD consistently fits to a much lower value of $\sim 1.29 \times 10^{-6}\,\text{Å}^{-2}$ as compared to the bulk value for CrSe of $3.6 \times 10^{-6}\,\text{Å}^{-2}$. A possible reason for this is the diffusion of Mn from the MnTe into the CrSe layer, whereby the negative SLD of Mn [27] reduces the overall scattering length density ($\text{SLD}_{\text{Mn}} = -3.071 \times 10^{-6}\,\text{Å}^{-2}$). This assumption is reasonable, given that MnTe was deposited at an elevated temperature of 370 °C, which may have enabled the diffusion of Mn into the CrSe layer. The CrSe layer is also consistently ~3.5 times thicker than the intended nominal thickness of 2.4 nm.

Third, the interface between Bi_2Te_3 and MnTe is not abrupt. The interface width is consistently determined to be ~2.2 nm, in contrast to the interfaces shown in similar systems by Katmis *et al.* [16] (for different materials) and akin to the very diffuse interfaces shown by He *et al.* [23]. The nSLD for the MnTe layer is very close to its bulk value. If there would be a significant Cr diffusion into the MnTe layer, this agreement would not be expected. The Bi_2Te_3 layer is consistently found to be more dense. On the one hand, this

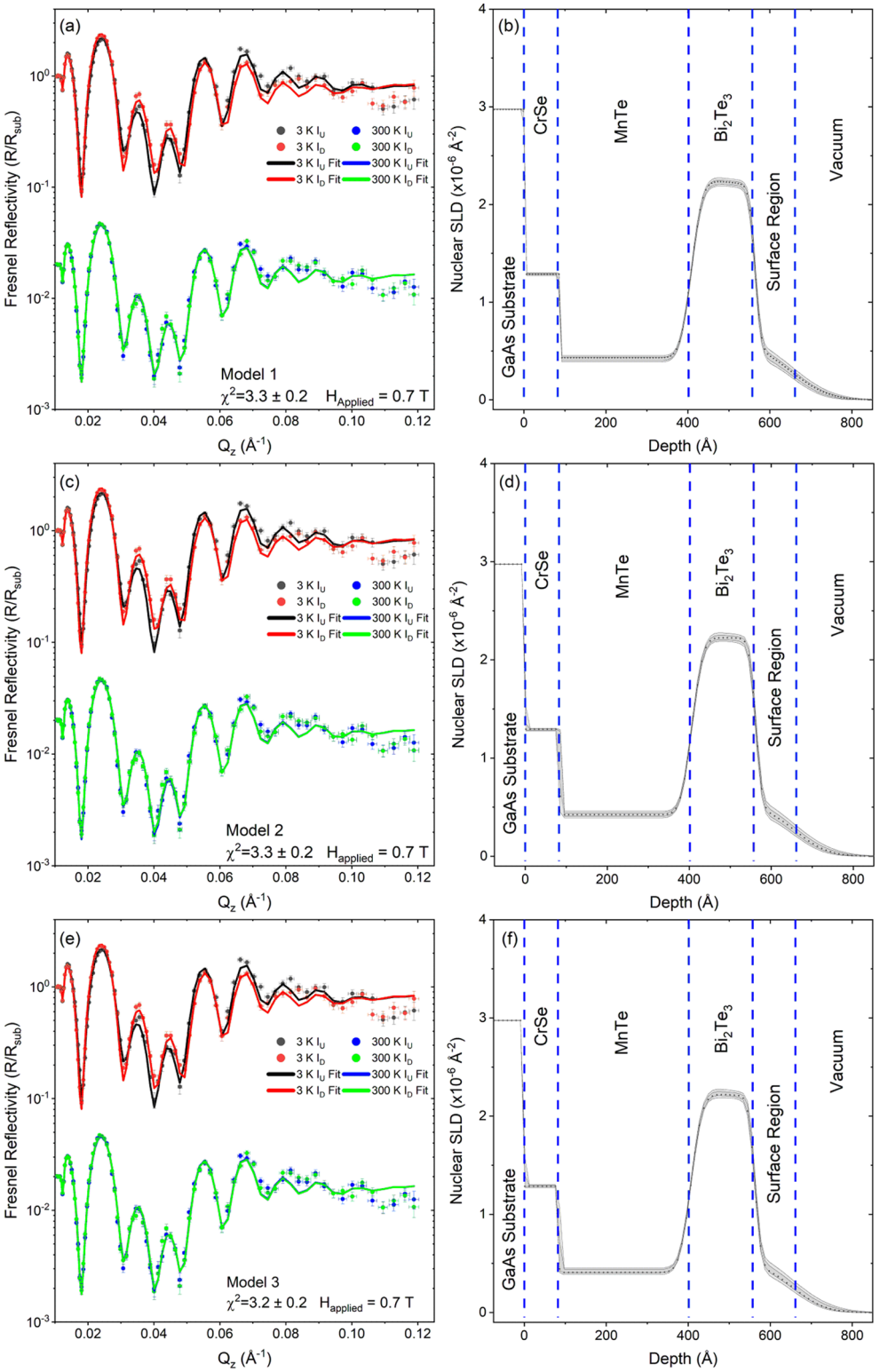

FIG. 2. PNR (nuclear structural information) of the CrSe/MnTe/Bi_2Te_3 trilayer stack as fitted by three different models. (a), (c), (e) Fresnel reflectivity and best fits for 3 and 300 K, respectively. (b), (d), (f) Full-scale nSLD profile. The gray regions represent the 95% Bayesian uncertainty intervals. Model 1 is the simplest possible case, with magnetism only in the CrSe buffer layer. In model 2, magnetism exists both in the CrSe and MnTe layer. In model 3, all layers are assumed to be magnetic.

implies that any potential Mn diffusion would be small in the Bi_2Te_3 layer as Mn would be expected to reduce the nSLD value; any Mn doping would have to be counteracted by a higher scattering length (SL) material than Bi_2Te_3. On the other hand, it gives a clear indication that the Bi_2Te_3 layer is not at the ideal elemental ratio neither. One possibility is that the Bi_2Te_3 was slightly Bi rich, leading to the increased nSLD observed here. The only other high SL materials present

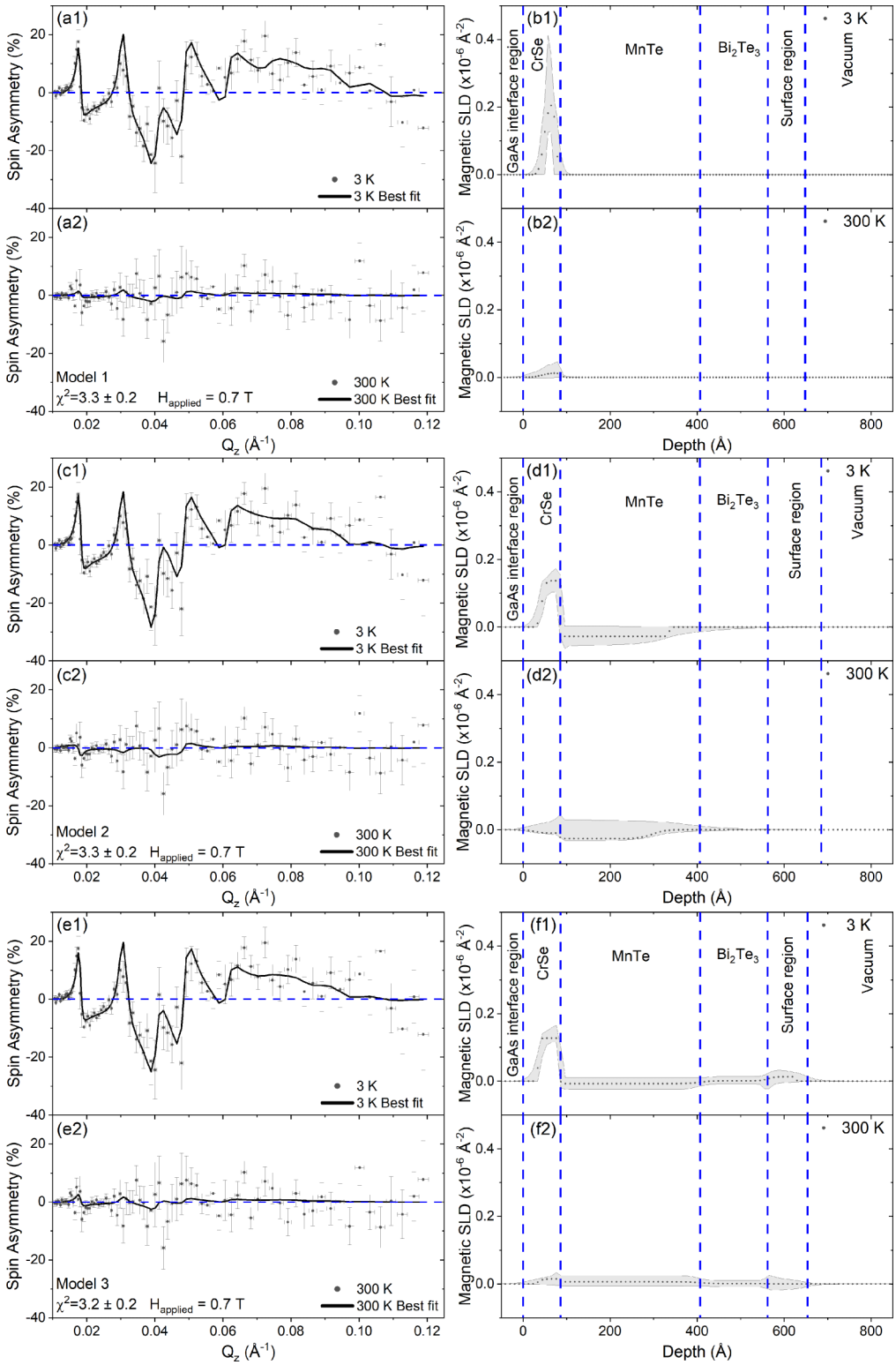

FIG. 3. PNR of the CrSe/MnTe/Bi_2Te_3 trilayer stack as fitted by three different models. The full nSLD profile, the Fresnel reflectivity curves, and a short description of the models can be found in Fig. 2. Plots of the spin asymmetry (SA) and corresponding magnetic scattering length density profiles (mSLD) are shown in (a), (c), (e) and (b), (d), (f), respectively. The upper panels show the 3 K and the lower panels the 300 K data sets and mSLD. The SA data sets were cofitted with all structural/nuclear parameters shared between the two temperatures. The gray regions represent the 95% Bayesian uncertainty intervals.

within the heterostructure that could increase the nSLD of this layer would be Cr or Se. Given that these elements would have to diffuse through the entire MnTe layer to reach the Bi_2Te_3, diffusion of Cr and Se is unlikely to be the cause.

Finally, a large diffusive interfacial region at the surface is required to get a good nuclear fit. This appears to be inherently linked to the GaAs substrate roughness. Atomic force microscopy of the layer stack exhibits a surface roughness of between 2–3 nm, superimposed on a larger-scale modulation with an amplitude of ∼20 nm (see Fig. S2 in the Supplemental Material [26]). On the other hand, the high quality of the nuclear fits shows that the $CrSe/MnTe/Bi_2Te_3$ heterostructure is remarkably conformal. The diffusive surface region is therefore a result of a highly conformal trilayer, following the substrate undulations, and the integration of the vacuum along with the Bi_2Te_3 surface region.

Figures 3(a), 3(c), and 3(e) show the spin asymmetry (SA) data and 3(b), 3(d), 3(f) the magnetic scattering length density profiles (mSLD) for three different models. The upper (lower) panels of each of those figures show data taken at $T = 3$ K (300 K), respectively. The SA is defined as $SA = (R_+ - R_-)/(R_+ + R_-)$ where R_+ and R_- are the spin-up and spin-down neutron specular reflectivities. The SA scales with the magnetism in the system. The blue dashed line acts as a guide to the eye, indicating zero magnetism. The mSLD profiles show the magnetic scattering density as a function of depth down from the surface of the sample. The banded regions represent the 95% Bayesian uncertainty intervals in the mSLD for the given model.

The first model shown in Figs. 3(a) and 3(b) follows the basic assumption that magnetism is only present in the CrSe layer. This produces an excellent match to the SA data at both 3 and 300 K with a moment close to the interface with the MnTe and a small reduced magnetism region close to the GaAs substrate. This is in line with Bose and Kudrnovský [28], where it was found that CrSe is ferromagnetic when deposited on GaAs(111)B substrates. However, as we detect a magnetically depleted region close to the GaAs(111)B interface, which, along with the reduced nSLD of the CrSe layer resulting from the suspected Mn diffusion, implies that the CrSe layer is not a simple binary FM. The magnitude of the moment significantly reduces at 300 K, as to be expected from the SQUID measurements (see Fig. S1 in the Supplemental Material [26]).

Model 2, shown in Figs. 3(c) and 3(d) allows for magnetism in both the CrSe and MnTe layers, which, however, does not improve the χ^2 figure of merit, indicating that the model is over-parametrized. This model again produces a clear nonzero magnetic moment in the CrSe layer near the interface with MnTe, along with a depleted or dead layer region at the interface with the GaAs(111)B substrate. A small, negative nonzero moment at 3 K is present in the MnTe layer, however, there is a large uncertainty as shown by the 95% confidence interval, which just crosses zero. This suggests that this model and the data support the existence of a nonzero moment in the MnTe with a statistical significance of slightly $<2\sigma$. However, this does not allow us to draw conclusions about the validity of this model over model 1. As in model 1, the moment in the CrSe becomes effectively zero at 300 K within the confidence bounds, as does any indication of moment in the MnTe.

Model 3, shown in Figs. 3(e) and 3(f), introduces magnetism in all the layers of the system, but only produces a marginal change in χ^2. The CrSe region is reproduced, and, as in model 2, nonzero moments are found in the MnTe layer. In contrast to the other models, nonzero moments can be observed in the Bi_2Te_3 and the surface region. However, since the 95% uncertainty intervals for the mSLD for both the MnTe and Bi_2Te_3 layers are far greater than the absolute values from the best fit and cross through zero, it cannot be stated that model 3 supports the existence of nonzero moments in these layers. Thus, it is not surprising that the moments are smaller than in case of model 2. In accordance with the other models, no indication of an induced magnetic moment at the $MnTe/Bi_2Te_3$ interface could be found. For the Q-range and counting statistics present within the data, the PNR results do not detect any presence of PIM in this particular sample - this is not surprising given the broad $MnTe/Bi_2Te_3$ interface width (∼2.2 nm; see Supplemental Material [26] for details) and the evidence of interdiffusion present within the heterostructure. As for models 1 and 2, the moments in all the layers become effectively zero at 300 K.

Other modeling was attempted to deliberately introduce PIM-like effects at the interface of the $MnTe/Bi_2Te_3$ layers (not shown), however, this produces either significantly worse fits or very large uncertainties in the interface region, preventing the models from converging.

In summary, it is difficult to evaluate the three models describing the magnetic profile of the $CrSe/MnTe/Bi_2Te_3$ layers. Their goodness-of-fit values from the Bayesian analysis of the PNR data are very close to each other. Given that a small nonzero ferromagnetic moment in the CrSe layer is consistently observed within all three models, there is strong evidence that this layer is indeed magnetic (albeit nonuniform with respect to depth). Beyond this, models 2 and 3 do not show significant evidence for nonzero moments in the other layers within the heterostructure. Consequently, none of the models supports the presence of PIM at the $MnTe/Bi_2Te_3$ interface. From model 2, the best fit value shows hints of antialigned ferromagnetism in the MnTe layer. However, this is not conclusive as determination of the mSLD in the MnTe layer and at the $MnTe/Bi_2Te_3$ interface are hampered by high uncertainty. Because of this, we performed element-selective x-ray spectroscopy using both total electron yield (TEY) and fluorescence yield (FY).

V. X-RAY SPECTROSCOPY

Starting with the Bi_2Te_3 layer, its contribution to the AHE is evidence that some form of magnetic order must be present in the nominally undoped, nonmagnetic TI. The likely candidates are unintentional Cr- or Mn-doping stemming from the migration of metal ions from the respective CrSe or MnTe layers into the TI. We employed element-selective x-ray absorption spectroscopy (XAS) using polarized x rays to shed light on this issue. By measuring the TEY, we are able to exclusively probe the uppermost layers, which is essentially the TI, i.e., contributions from the CrSe and MnTe layers which are buried deeper under the surface are not detected. No sign of Cr can be found in the TI [see Figs. 4(c) and 4(d)]. Instead, the spectra show a contribution at the Te M_5 edge

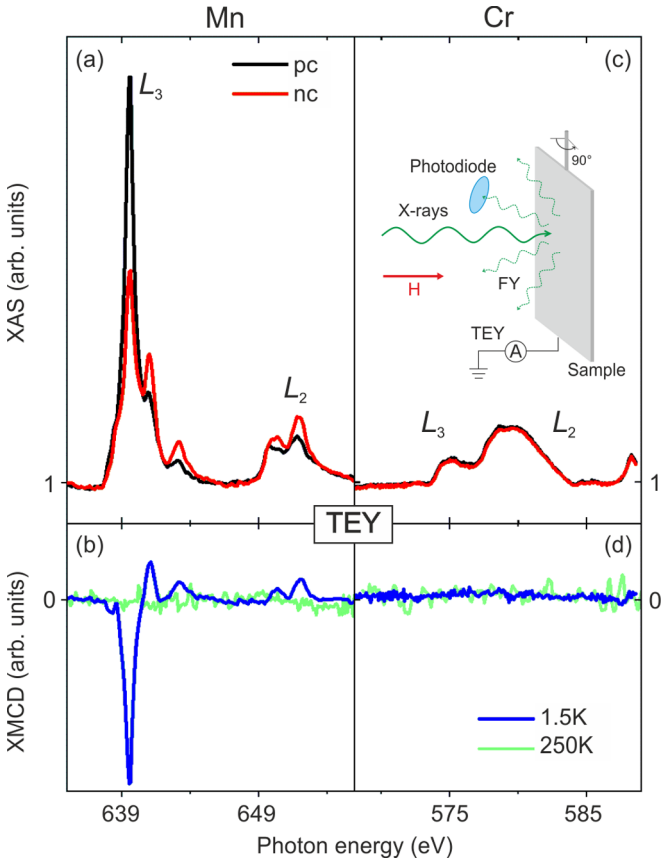

FIG. 4. (a), (c) XAS and (b), (d) XMCD at the Mn and Cr $L_{2,3}$ edges measured in surface-sensitive total electron yield (TEY) mode. The measurements were carried out at 1.5 and 250 K, but only the XAS at 1.5 K for both positive (pc) and negative circular (nc) helicity is shown. A magnetic field of 6 T was applied along the incident x-ray direction, perpendicular to the sample plane, to saturate the magnetization of the sample. The geometry of the setup and available detectors is shown in the inset in (c).

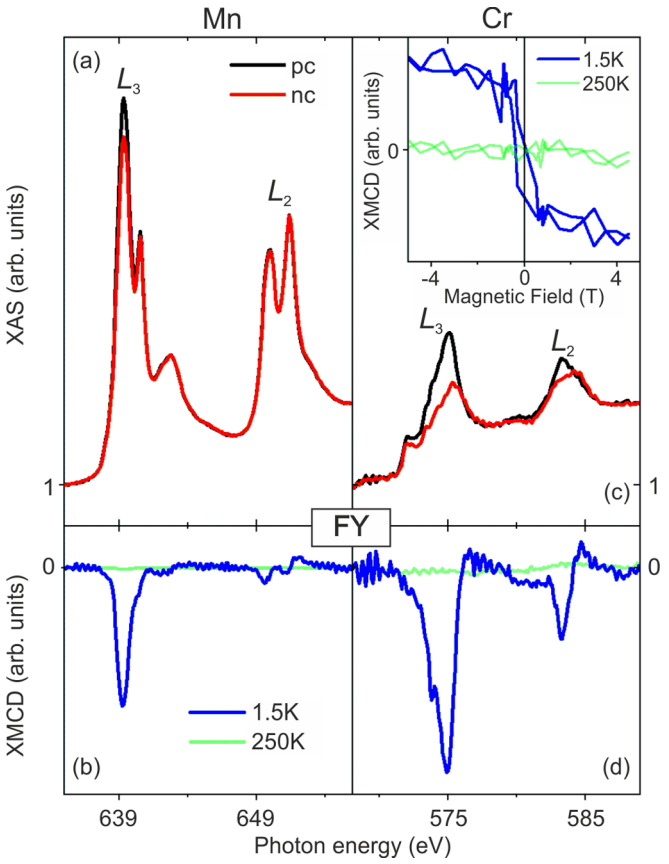

FIG. 5. (a), (c) XAS and (b), (d) XMCD at the Mn and Cr $L_{2,3}$ edges measured in fluorescence yield (FY). The inset in (c) shows the out-of-plane XMCD hysteresis at the Cr L_3 edge at 1.5 and at 250 K.

(compare to Fig. 3(d) in Ref. [29]). An XAS spectrum typical for the Mn $L_{2,3}$ edges can be seen in Fig. 4(a). Moreover, the nonzero x-ray magnetic circular dichroism (XMCD) at 1.5 K is evidence for ferromagnetic ordering due to the magnetic Mn doping of the TI. This is commensurate with model 3 where a slight nonzero magnetic moment was observed in the surface region of the TI at 3 K, but not in its bulk [see Fig. 3(f1)]. The Mn-XMCD disappears at 250 K [see Fig. 4(b)], matching well with the change in transport properties shown in Fig. 1. The diffusion of Mn into the TI can take place firstly along grain boundaries, i.e., vertically, followed by horizontal diffusion along the van der Waals gap [30,31]. Mn has been shown to enter Bi_2Te_3 interstitially instead of substitutionally [32], precluding the formation of a $MnBi_2Te_4$ phase. The spectral line shape allows us to identify the local electron state of the ground state. Different electron configurations give markedly different spectral shapes [33]. The shape of the Mn XMCD in TEY [see Fig. 5(b)] agrees well with that of Mn-doped Bi_2Te_3 with Mn in the 2+ state [32].

The PNR results did not provide evidence for Mn in the Bi_2Te_3 layer. However, XMCD in TEY is very surface sensitive and the observed signal is an indication for trace amounts of Mn within the first few nm of the sample surface [34]. Assuming such a very low concentration of Mn in the immediate vicinity of the surface, it is not surprising that PNR does not pick up its presence.

CrSe has been reported to be antiferromagnetically ordered [35,36], but calculations have shown that ferromagnetic order is possible, depending on the lattice spacing [28,37,38]. In particular, if the CrSe layer is lattice matched to the GaAs(111)B substrate, a ferromagnetic state might be expected [28]. We demonstrate the latter using element-specific XAS by showing a nonzero XMCD signal at the Cr $L_{2,3}$ edge. Measurements in FY mode provide information about the layers deeper down in the sample. Here, Cr-XMCD can be detected although the signal is quite weak [see Fig. 5(d)], suggesting that CrSe is, or at least a fraction of the film, ferromagnetically ordered. Another potential source of the XMCD is ferromagnetic $Mn_{1-x}Cr_xTe$ due to migration of Cr into the MnTe layer [39–41]. Nevertheless, a substantial level of doping of >10% would be required, which is rather unlikely, and the fitted PNR nSLD value for the MnTe agrees well with the bulk value. For lower doping levels, an antiferromagnetic phase was observed [42], in agreement with theoretical calculations [43]. To explore the magnetic state of the CrSe layer further, field-dependent XMCD scans were carried out at the Cr-L_3 edge [see inset in Fig. 5(c)]. At 1.5 K, a hysteresis is observed, which clearly proves that the

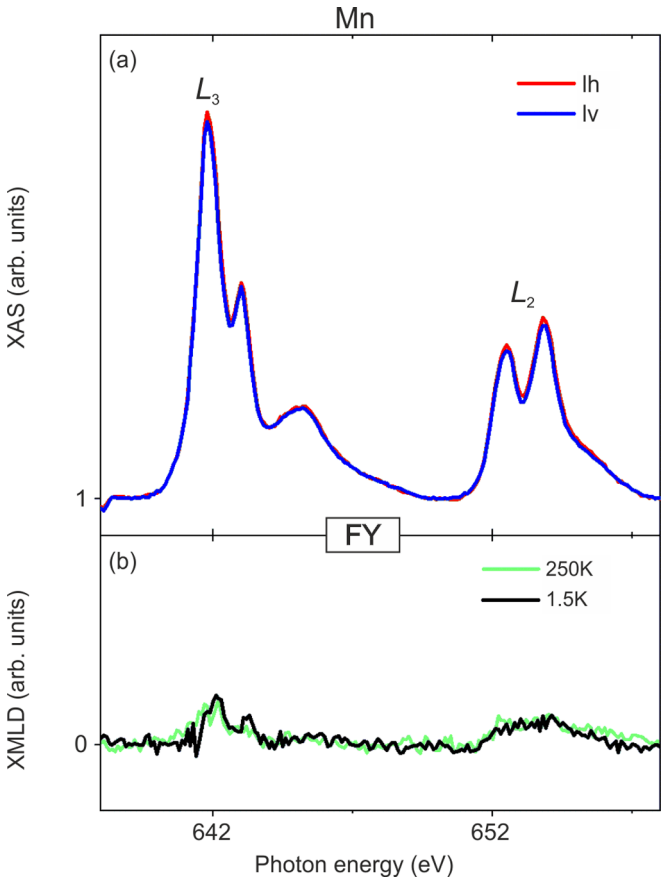

FIG. 6. XMLD at the Mn $L_{2,3}$ edges in FY mode. (a) XAS for linear horizontal (lh) and linear vertical (lv) polarization at 1.5 K, and (b) XMLD spectra. The incidence angle of the x rays was perpendicular to the sample surface to probe the in-plane component of the antiferromagnetic vector. No magnetic field was applied.

CrSe layer is ferromagnetic. Because of the small and noisy signal, it is difficult to gain quantitative information about the coercivity and magnetic anisotropy. No hysteresis is visible at 250 K, in line with the static XMCD measurements.

What remains is the question about the magnetic state of the MnTe layer, where both magnetoresistance and PNR measurements hint at traces of ferromagnetism. This stands in opposition to the fact that, in principle, the most stable phase of MnTe under atmospheric conditions is α-MnTe, an A-type semiconducting AFM with a Néel temperature of 310 K [44]. We expect Mn $L_{2,3}$ XMLD spectra comparable to those of Ref. [45], where the integrated signal over each edge vanishes for Mn^{2+}. Instead, however, the spectrum in Fig. 6(b) shows a nonvanishing signal with definite sign. The fact that the XMLD resembles the shape of the XAS spectra [see Fig. 6(a)] points to an artifact resulting from drift. However, a nonzero XMCD at the Mn $L_{2,3}$ edges cannot be interpreted as resulting from drift, since the characteristic sign change between the two edges is observed [see Fig. 5(b)]. What is more important, when a magnetic field with opposite sign is applied, the XMCD contrast inverts (not shown here), providing further evidence for a magnetic origin. Both XMLD and XMCD were taken with the x rays perpendicular to the sample plane. Hence, evidence for an in-plane antiferromagnetic spin orientation, as predicted for α-MnTe, could not be found. The XMLD measurement was repeated with the beam at 60° with respect to the sample normal to check for an out-of-plane antiferromagnetic orientation, but no XMLD could be detected as well (not shown here). The failure to detect a measurable XMLD is in itself not proof for the absence of antiferromagnetism in the MnTe layer since the effect could be too small to be detected in a layer buried deep within the sample. The XMCD observed in the FY [see Fig. 5(b)] can be explained in several ways, and the likelihood of a ferromagnetic phase in the MnTe layer will be discussed in the following.

First, it has to be noted that the majority of experiments [25,44] and theoretical calculations report the observation of a NiAs-type hexagonal α-phase in which MnTe is antiferromagnetic [46]. Besides this phase, MnTe can be found in a wurtzite-type hexagonal β phase, zincblende γ phase, or rocksalt δ phase. A switching between these phases by reversible polymorphic transformations has been reported [47]. Temperature or strain could act as trigger for a phase change [48]. Furthermore, Watanabe *et al.* [49] observed a partial structural change of MnTe in MnTe/InP heterostructures and found a small subsection of the MnTe film to exhibit both ferromagnetism and conductivity. The latter would conveniently explain the AHE effect observed.

In addition, it is possible that the Mn dopants in the Bi_2Te_3 layer, the source of the XMCD observed in the TEY, contributes to the XMCD measured in FY as well. The analysis of the Mn $L_{2,3}$ peaks, however, is hampered by the well-known self-absorption effect in thick layers when using the FY mode, often expressing itself as dips in the spectra instead of absorption peaks [50]. A sensible sum rules analysis from which meaningful, quantitative values of the magnetization in the MnTe layer could be derived is unfortunately not possible. The TEY mode, on the other hand, is not affected by this shortcoming, however, it is unable to probe such deeply buried layers as the MnTe layer.

VI. SUMMARY

We presented a comprehensive study of a TI proximity coupled to a magnetically ordered system using magnetotransport, PNR, and x-ray spectroscopy. We studied the magnetic properties of $CrSe/MnTe/Bi_2Te_3$ heterostructures and confirmed that CrSe is ferromagnetic and that Bi_2Te_3 is, at least partially, unintentionally doped with Mn. The transport, as well as the x-ray spectroscopy data, suggest that the MnTe layer is not in its often-desired antiferromagnetic phase. The XMCD signal stemming from within the bulk of the sample could be an indication of a ferromagnetic phase in the MnTe layer, however, other explanations are possible, such as Mn doping of the CrSe or Bi_2Te_3 layer.

Finally, the magnetic depth profile of the trilayer was probed at 3 and 300 K using depth-sensitive PNR. Importantly, no indications for PIM could be found, independent of the model used for the PNR fits. We conclude that the magnetic landscape in TI-magnetic layer heterostructures is more complex than often assumed. Given that the magnetic moments in such systems can be very small, neutron-based techniques such as PNR are clearly at the limit for the counting statistics within the available time. Sufficient

statistics is critical so the highly complex multiparameter fit models for the PNR data can provide reliable results. As we have shown, magnetotransport and x-ray spectroscopy are ideally suited to complement the PNR measurements. Only with the additional information provided were we able to exclude the formation of an induced magnetization at the interface of the TI-magnetic layer interface. The complexity of these systems, and the large sensitivity to interfacial effects, explains why so far the elusive QAH effect has not been found in such systems. A better understanding and control of the magnetic properties of TI-magnetic layer heterostructures has to be gained to be able to optimize these in principle promising systems for future quantum applications at ambient temperatures.

ACKNOWLEDGMENTS

This work is sponsored by the National Key R&D Program of China under Contract No. 2017YFB0405704, the National Natural Science Foundation of China (Grant No. 61874172), and the Major Project of Shanghai Municipal Science and Technology (Grant No. 2018SHZDZX02). Q.Y. acknowledges the support from the Shanghai Sailing Program (Grant No. 19YF1433200) and the National Natural Science Foundation of China (Grant No. 11904230). X.K. acknowledges the support from the Strategic Priority Research Program of Chinese Academy of Sciences (Grant No. XDA18010000). A.F., G.v.d.L., and T.H. acknowledge funding from the Engineering and Physical Sciences Research Council (No. EP/P020151/1 and No. EP/P021190/1) and the Oxford-ShanghaiTech collaboration project. We acknowledge Diamond Light Source for beamtime at the I06 branchline under Proposal No. MM23748. We also acknowledge the ISIS muon and neutron source for beamtime on POLREF under Proposals No. RB1820603 and No. RB1910543, and for computing resources provided by STFC Scientific Computing Department's SCARF cluster. The data that support the findings of this study are available via Refs. [53,54].

[1] F. D. M. Haldane, Model for a Quantum Hall Effect Without Landau Levels: Condensed-Matter Realization of the Parity Anomaly, Phys. Rev. Lett. **61**, 2015 (1988).

[2] C. Z. Chang, J. Zhang, X. Feng, J. Shen, and Z. Zhang, Experimental observation of the quantum anomalous Hall effect in a magnetic topological insulator, Science **340**, 167 (2013).

[3] Y. L. Chen, J.-H. Chu, J. G. Analytis, Z. K. Liu, K. Igarashi, H.-H. Kuo, X. L. Qi, S. K. Mo, R. G. Moore, D. H. Lu, M. Hashimoto, T. Sasagawa, S. C. Zhang, I. R. Fisher, Z. Hussain, and Z. X. Shen, Massive Dirac fermion on the surface of a magnetically doped topological insulator, Science **329**, 659 (2010).

[4] L. Fu and C. L. Kane, Superconducting Proximity Effect and Majorana Fermions at the Surface of a Topological Insulator, Phys. Rev. Lett. **100**, 096407 (2008).

[5] B. Lian, X.-Q. Sun, A. Vaezi, X.-L. Qi, and S.-C. Zhang, Topological quantum computation based on chiral Majorana fermions, Proc. Natl. Acad. Sci. **115**, 10938 (2018).

[6] K. von Klitzing, G. Dorda, and M. Pepper, New Method for High-Accuracy Determination of the Fine-Structure Constant Based on Quantized Hall Resistance, Phys. Rev. Lett. **45**, 494 (1980).

[7] C.-Z. Chang, W. Zhao, D. Y. Kim, H. Zhang, B. A. Assaf, D. Heiman, S.-C. Zhang, C. Liu, M. H. W. Chan, and J. S. Moodera, High-precision realization of robust quantum anomalous Hall state in a hard ferromagnetic topological insulator, Nat. Mater. **14**, 473 (2015).

[8] J. G. Checkelsky, J. Ye, Y. Onose, Y. Iwasa, and Y. Tokura, Dirac-fermion-mediated ferromagnetism in a topological insulator, Nat. Phys. **8**, 729 (2012).

[9] J. G. Checkelsky, R. Yoshimi, A. Tsukazaki, K. S. Takahashi, Y. Kozuka, J. Falson, M. Kawasaki, and Y. Tokura, Trajectory of the anomalous Hall effect towards the quantized state in a ferromagnetic topological insulator, Nat. Phys. **10**, 731 (2014).

[10] L. B. Duffy, N. Steinke, J. A. Krieger, A. I. Figueroa, K. Kummer, T. Lancaster, S. R. Giblin, F. L. Pratt, S. J. Blundell, T. Prokscha, A. Suter, S. Langridge, V. N. Strocov, Z. Salman, G. van der Laan, and T. Hesjedal, Microscopic effects of Dy doping in the topological insulator Bi_2Te_3, Phys. Rev. B **97**, 174427 (2018).

[11] L. B. Duffy, A. Frisk, D. M. Burn, N. J. Steinke, J. Herrero-Martin, A. Ernst, G. van der Laan, and T. Hesjedal, Imposing long-range ferromagnetic order in rare-earth-doped magnetic topological-insulator heterostructures, Phys. Rev. Materials **2**, 054201 (2018).

[12] L. B. Duffy, N. J. Steinke, D. M. Burn, A. Frisk, L. Lari, B. Kuerbanjiang, V. K. Lazarov, G. van der Laan, S. Langridge, and T. Hesjedal, Magnetic profile of proximity-coupled (Dy, $BiTe)_3$/(Cr, $SbTe)_3$ topological insulator heterostructures, Phys. Rev. B **100**, 054402 (2019).

[13] P. Wei, F. Katmis, B. A. Assaf, H. Steinberg, P. Jarillo-Herrero, D. Heiman, and J. S. Moodera, Exchange-Coupling-Induced Symmetry Breaking in Topological Insulators, Phys. Rev. Lett. **110**, 186807 (2013).

[14] M. Li, C. Z. Chang, B. J. Kirby, M. E. Jamer, W. Cui, L. Wu, P. Wei, Y. Zhu, D. Heiman, J. Li, and J. S. Moodera, Proximity-Driven Enhanced Magnetic Order at Ferromagnetic-Insulator-Magnetic-Topological-Insulator Interface, Phys. Rev. Lett. **115**, 087201 (2015).

[15] M. Li, W. Cui, J. Yu, Z. Dai, Z. Wang, F. Katmis, W. Guo, and J. Moodera, Magnetic proximity effect and interlayer exchange coupling of ferromagnetic/topological insulator/ferromagnetic trilayer, Phys. Rev. B **91**, 014427 (2015).

[16] F. Katmis, V. Lauter, F. S. Nogueira, B. A. Assaf, M. E. Jamer, P. Wei, B. Satpati, J. W. Freeland, I. Eremin, D. Heiman, P. Jarillo-Herrero, and J. S. Moodera, A high temperature ferromagnetic topological insulating phase by proximity coupling, Nature **533**, 513 (2016).

[17] Y. Deng, Y. Yu, M. Z. Shi, Z. Guo, Z. Xu, J. Wang, X. H. Chen, and Y. Zhang, Quantum anomalous Hall effect in intrinsic magnetic topological insulator $MnBi_2Te_4$, Science **367**, 895 (2020).

[18] M. Mogi, R. Yoshimi, A. Tsukazaki, K. Yasuda, Y. Kozuka, K. S. Takahashi, M. Kawasaki, and Y. Tokura, Magnetic modulation doping in topological insulators toward higher-

temperature quantum anomalous Hall effect, Appl. Phys. Lett. **107**, 182401 (2015).

[19] I. Lee, C. K. Kim, J. Lee, S. J. Billinge, R. Zhong, J. A. Schneeloch, T. Liu, T. Valla, J. M. Tranquada, G. Gu, and J. C. Davis, Imaging Dirac-mass disorder from magnetic dopant atoms in the ferromagnetic topological insulator $Cr_x(Bi_{0.1}Sb_{0.9})_{2-x}Te_3$, Proc. Natl. Acad. Sci. **112**, 1316 (2015).

[20] R. Watanabe, R. Yoshimi, M. Kawamura, M. Mogi, A. Tsukazaki, X. Z. Yu, K. Nakajima, K. S. Takahashi, M. Kawasaki, and Y. Tokura, Quantum anomalous Hall effect driven by magnetic proximity coupling in all-telluride based heterostructure, Appl. Phys. Lett. **115**, 102403 (2019).

[21] S. V. Eremeev, V. N. Men'shov, V. V. Tugushev, P. M. Echenique, and E. V. Chulkov, Magnetic proximity effect at the three-dimensional topological insulator/magnetic insulator interface, Phys. Rev. B **88**, 144430 (2013).

[22] Q. L. He, X. Kou, A. J. Grutter, G. Yin, L. Pan, X. Che, Y. Liu, T. Nie, B. Zhang, S. M. Disseler, B. J. Kirby, W. Ratcliff, Q. Shao, K. Murata, X. Zhu, G. Yu, Y. Fan, M. Montazeri, X. Han, J. A. Borchers *et al.*, Tailoring exchange couplings in magnetic topological-insulator/antiferromagnet heterostructures, Nat. Mater. **16**, 94 (2017).

[23] Q. L. He, G. Yin, A. J. Grutter, L. Pan, X. Che, G. Yu, D. A. Gilbert, S. M. Disseler, Y. Liu, P. Shafer, B. Zhang, Y. Wu, B. J. Kirby, E. Arenholz, R. K. Lake, X. Han, and K. L. Wang, Exchange-biasing topological charges by antiferromagnetism, Nat. Commun. **9**, 2767 (2018).

[24] Q. L. He, G. Yin, L. Yu, A. J. Grutter, L. Pan, C.-Z. Chen, X. Che, G. Yu, B. Zhang, Q. Shao, A. L. Stern, B. Casas, J. Xia, X. Han, B. J. Kirby, R. K. Lake, K. T. Law, and K. L. Wang, Topological Transitions Induced by Antiferromagnetism in a Thin-Film Topological Insulator, Phys. Rev. Lett. **121**, 096802 (2018).

[25] P. Chen, Y. Zhang, Q. Yao, F. Tian, L. Li, Z. Qi, X. Liu, L. Liao, C. Song, J. Wang, J. Xia, G. Li, D. M. Burn, G. van der Laan, T. Hesjedal, S. Zhang, and X. Kou, Tailoring the hybrid anomalous Hall response in engineered magnetic topological insulator heterostructures, Nano Lett. **20**, 1731 (2020).

[26] See Supplemental Material at http://link.aps.org/supplemental/10.1103/PhysRevMaterials.6.053402 for (the structural model, fits to reflectivity and spin asymmetry, spin asymmetry with and without magnetization from the PIM layer, the comparison of the MSLD with and without PIM, and fitting using Refl1D) containing Refs. [51,52].

[27] https://www.ncnr.nist.gov/resources/n-lengths/, accessed Dec. 15, 2021.

[28] S. K. Bose and J. Kudrnovský, Exchange interactions and Curie temperatures in Cr-based alloys in the zinc blende structure: Volume- and composition-dependence from first-principles calculations, Phys. Rev. B **81**, 054446 (2010).

[29] A. I. Figueroa, F. Bonell, M. G. Cuxart, M. Valvidares, P. Gargiani, G. van der Laan, A. Mugarza, and S. O. Valenzuela, Absence of Magnetic Proximity Effect at the Interface of Bi_2Se_3 and (Bi, Sb)$_2$Te$_3$ with EuS, Phys. Rev. Lett. **125**, 226801 (2020).

[30] A. Ghasemi, D. Kepaptsoglou, A. I. Figueroa, G. A. Naydenov, P. J. Hasnip, M. I. Probert, Q. Ramasse, G. van der Laan, T. Hesjedal, and V. K. Lazarov, Experimental and density functional study of Mn doped Bi_2Te_3 topological insulator, APL Mater. **4**, 126103 (2016).

[31] A. I. Figueroa, T. Hesjedal, and N.-J. Steinke, Magnetic order in 3D topological insulators–Wishful thinking or gateway to emergent quantum effects? Appl. Phys. Lett. **117**, 150502 (2020).

[32] M. D. Watson, L. J. Collins-Mcintyre, L. R. Shelford, A. I. Coldea, D. Prabhakaran, S. C. Speller, T. Mousavi, C. R. Grovenor, Z. Salman, S. R. Giblin, G. van der Laan, and T. Hesjedal, Study of the structural, electric and magnetic properties of Mn-doped Bi_2Te_3 single crystals, New J. Phys. **15**, 103016 (2013).

[33] G. van der Laan and B. T. Thole, Strong magnetic x-ray dichroism in $2p$ absorption spectra of $3d$ transition-metal ions, Phys. Rev. B **43**, 13401 (1991).

[34] G. van der Laan, Applications of soft x-ray magnetic dichroism, J. Phys.: Conf. Ser. **430**, 012127 (2013).

[35] M. Koyama, N. Happo, M. Tamura, J. Harada, T. Mihara, A. Furuta, M. Nakatake, H. Sato, M. Taniguchi, and Y. Ueda, Photoemission and ultraviolet inverse-photoemission studies of CrSe with NiAs-type crystal structure, J. Electron Spectrosc. Relat. Phenom. **78**, 83 (1996).

[36] C. Wang, B. Zhang, B. You, S. K. Lok, S. K. Chan, X. X. Zhang, G. K. Wong, and I. K. Sou, Competitive antiferromagnetic and ferromagnetic coupling in a CrSe/Fe/GaAs(111)B structure, J. Appl. Phys. **104**, 023916 (2008).

[37] K. Nakamura, Y. Kato, T. Akiyama, T. Ito, and A. J. Freeman, Half-Metallic Exchange Bias Ferromagnetic/Antiferromagnetic Interfaces in Transition-Metal Chalcogenides, Phys. Rev. Lett. **96**, 047206 (2006).

[38] L. Xiong, L. Yi, and G. Y. Gao, Surface half-metallicity and stability of zinc-blende CrSe: A comprehensive first-principles study, J. Magn. Magn. Mater. **349**, 69 (2014).

[39] Y. B. Li, Y. Q. Zhang, N. K. Sun, Q. Zhang, D. Li, J. Li, and Z. D. Zhang, Ferromagnetic semiconducting behavior of $Mn_{1-x}Cr_xTe$ compounds, Phys. Rev. B **72**, 193308 (2005).

[40] Z. H. Wang, D. Y. Geng, W. J. Gong, J. Li, Y. B. Li, and Z. D. Zhang, Effect of adding Cr on magnetic properties and metallic behavior in MnTe film, Thin Solid Films **522**, 175 (2012).

[41] Z. H. Wang, D. Y. Geng, J. Li, Y. B. Li, and Z. D. Zhang, Magnetic and transport properties of $Mn_{0.98}Cr_{0.02}Te$ epitaxial films grown on Al_2O_3 substrates, J. Mater. Sci. Technol. **30**, 103 (2014).

[42] M. M. H. Polash, M. Rasoulianboroujeni, and D. Vashaee, Magnon and spin transition contribution in heat capacity of ferromagnetic Cr-doped MnTe: Experimental evidence for a paramagnetic spin-caloritronic effect, Appl. Phys. Lett. **117**, 043903 (2020).

[43] N. H. Long and H. Akai, Ab-initio calculation of electronic and magnetic properties of $Mn_{1-x}Cr_xTe$, J. Supercond. Nov. Magn. **20**, 473 (2007).

[44] D. Kriegner, K. Vyborny, K. Olejník, H. Reichlova, V. Novak, X. Marti, J. Gazquez, V. Saidl, P. Nemec, V. Volobuev, G. Springholz, V. Holy, and T. Jungwirth, Multiple-stable anisotropic magnetoresistance memory in antiferromagnetic MnTe, Nat. Commun. **7**, 11623 (2016).

[45] A. A. Freeman, K. W. Edmonds, G. van der Laan, N. R. Farley, T. K. Johal, E. Arenholz, R. P. Campion, C. T. Foxon, and B. L. Gallagher, Giant anisotropy in x-ray magnetic linear dichroism in (Ga, Mn)As, Phys. Rev. B **73**, 233303 (2006).

[46] M. Krause and F. Bechstedt, Structural and magnetic properties of MnTe phases from ab initio calculations, J. Supercond. Nov. Magn. **26**, 1963 (2013).

[47] S. Mori, S. Hatayama, Y. Shuang, D. Ando, and Y. Sutou, Reversible displacive transformation in MnTe polymorphic semiconductor, Nat. Commun. **11**, 85 (2020).

[48] W. Kim, I. J. Park, H. J. Kim, W. Lee, S. J. Kim, and C. S. Kim, Room-temperature ferromagnetic property in MnTe semiconductor thin film grown by molecular beam epitaxy, IEEE Trans. Magn. **45**, 2424 (2009).

[49] R. Watanabe, R. Yoshimi, M. Shirai, T. Tanigaki, M. Kawamura, A. Tsukazaki, K. S. Takahashi, R. Arita, M. Kawasaki, and Y. Tokura, Emergence of interfacial conduction and ferromagnetism in MnTe/InP, Appl. Phys. Lett. **113**, 181602 (2018).

[50] S. Eisebitt, T. Boske, J.-E. Rubensson, and W. Eberhard, Determination of absorption coefficients for concentrated samples by fluorescence detection, Phys. Rev. B **47**, 14103 (1993).

[51] A. Koutsioubas, Model-independent recovery of interfacial structure from multi-contrast neutron reflectivity data, J. Appl. Crystallogr. **52**, 538 (2019).

[52] F. Abelés, The general theory of thin films, J. Phys. Radium **11**, 307 (1950).

[53] https://doi.org/10.5286/ISIS.E.RB1820603.

[54] https://doi.org/10.5286/ISIS.E.RB1910534.